Possible high COVID-19 airborne infection risk in deep and poorly ventilated 2D street canyons

Vitor Lavor[1], Omduth Coceal[2], Sue Grimmond[2], Jian Hang[3], Zhiwen Luo[4] (✉)

1. School of the Built Environment, University of Reading, Reading, UK
2. Department of Meteorology, University of Reading, Reading, UK
3. School of Atmospheric Sciences, Guangdong Province Key Laboratory for Climate Change and Natural Disaster Studies, Sun Yat-sen University, Guangzhou, China
4. Welsh School of Architecture, Cardiff University, Cardiff, UK

Abstract

Despite the widespread assumption that outdoor environments provide sufficient ventilation and dilution capacity to mitigate the risk of COVID-19 infection, there is little understanding of airborne infection risk in outdoor urban areas with poor ventilation. To address this gap, we propose a modified Wells-Riley model based on the purging flow rate (Q_{PFR}), by using computational fluid dynamics (CFD) simulations. The model quantifies the outdoor risk in 2D street canyons with different approaching wind speeds, urban heating patterns and aspect ratios (building height to street width). We show that urban morphology plays a critical role in controlling airborne infectious disease transmission in outdoor environments, especially under calm winds; with deep street canyons (aspect ratio > 3) having a similar infection risk as typical indoor environments. While ground and leeward wall heating could reduce the risk, windward heating (e.g., windward wall ~10 K warmer than the ambient air) can increase the infection risk by up to 75%. Our research highlights the importance of considering outdoor infection risk and the critical role of urban morphology in mitigating airborne infection risk. By identifying and addressing these risks, we can inform measures that may enhance public health and safety, particularly in densely populated urban environments.

1 Introduction

The coronavirus disease (COVID-19) pandemic caused by the SARS-CoV-2 virus has threatened lives and livelihoods globally. As of February 6th, 2023, the World Health Organization reported over 750 million confirmed cases globally, along with more than 6.8 million associated fatalities (WHO 2023). In terms of disease transmission, scientific evidence suggests the airborne transmission route plays a significant role in the spread of COVID-19 (Cheng et al. 2022), and the current understanding of the COVID-19 pandemic suggests that indoor spaces with poor ventilation, such as in religious events, restaurants, and public transport (James et al. 2020; Li et al. 2021; Cheng et al. 2022), are the main contributors to virus transmission.

There is a general consensus in the literature that airborne transmission risk in outdoor places is low primarily due to sufficient ventilation, adequate physical distancing between people and limited exposure time (cf. indoor environments) (Bulfone et al. 2021). However, outdoor locations are affected by transient atmospheric conditions of variables (e.g., wind speed, temperature and relative humidity), which are known to play an essential role in airborne transmission risk (Bourouiba 2020). The effectiveness of ventilation in reducing the concentration of airborne particles and the associated infection risk depends on various factors, including wind and buoyancy-driven ventilation (Mei and Yuan 2022). The ventilation rate and pattern, however, are not uniform among outdoor locations due to the complex and diverse urban morphologies that

E-mail: luoz18@cardiff.ac.uk

List of symbols

AR	aspect ratio $= H/W$ [—], Sections 2–3
c	concentration [kg m^{-3}], Eq. (3)
$<\overline{c}>$	spatial and temporal mean concentration [kg m^{-3}], Eq. (11)
FAC2	factor-of-2 of observations [—], Section 3.1
g	gravitational acceleration [m s^{-2}], Eq. (2)
H	building height [m], Section 2.2
I	number of infectors [person], Eqs. (9)–(10)
K_c	turbulent diffusivity of pollutant [m^2 s^{-1}], Eq. (3)
k	turbulent kinetic energy [m^2 s^{-2}], Eqs. (5)–(8)
N	number of data points [—], Eqs. (12)–(13)
nMAE	normalised mean absolute error [—], Eq. (14)
nMBE	normalised mean bias error [—], Eq. (16)
nMSE	normalised mean squared error [—], Eq. (15)
O_i	observed wind tunnel values [—], Eqs. (12)–(16)
P	pressure [Pa], Eq. (2)
P_i	simulations predicted values [—], Eqs. (12)–(16)
P_{indoor}	indoor infection risk [%], Eq. (9)
$P_{outdoor}$	outdoor infection risk [%], Eq. (10)
p	pulmonary ventilation rate [m^3 s^{-1}], Eqs. (9)–(10)
Q	ventilation rate with clean air [m^3 s^{-1}], Eq. (9)
Q_{PFR}	purging flow rate [m^3 s^{-1}], Eqs. (10)–(11)
Q_{min}	minimum ventilation rate with clean air [m^3 s^{-1}], Fig. 9
q	quanta generation rate [quanta (person s)$^{-1}$], Eqs. (9)–(10)
R	Pearson correlation coefficient [—], Eq. (13)

S_c	tracer emission rate [kg (m^3 s)$^{-1}$], Eqs. (3), (11)
Sc_t	Schmidt number [—], Section 2.1
T	temperature [K], Section 2.1
T_{ref}	reference temperature (=293.15 K), Section 2.1
TKE	turbulent kinetic energy [m^2 s^{-2}], Section 3.1
t	exposure time interval [s], Eqs. (9)–(10)
u	velocity [m s^{-1}], Section 3.1
u_i, u_j	velocity components [m s^{-1}], Eqs. (1)–(4)
u_{ref}	approaching wind speed [m s^{-1}], Sections 2–3
$\overline{u_i' u_j'}$	Reynolds stress [m^2 s^{-2}], Eqs. (2), (5)
V	volume where the tracer gas is homogeneously emitted [m^3], Eq. (11)
W	street width [m], Section 2
W_a	allowed absolute deviation [—], Eq. (12)
x_i, x_j	Cartesian coordinates [m], Section 2.1
y^+	wall–first node non-dimensional distance [—], Section 2.2
β	thermal expansion coefficient [K^{-1}], Section 2.1
γ	ventilation rate factor [—], Fig. 9
δ_{ij}	Kronecker delta [—], Eq. (5)
ε	turbulent kinetic energy dissipation rate [m^2 s^{-3}], Eqs. (6)–(8)
θ	potential temperature [K], Eq. (4)
ν	kinematic viscosity [m^2 s^{-1}], Section 2.1
ν_t	turbulent kinematic viscosity [m^2 s^{-1}], Eqs. (5)–(6)
ρ	fluid density [kg m^{-3}], Eq. (2)
ρ_0	reference fluid density (=1.225 kg m^{-3}), Eq. (2)

exist in different regions (Qin et al. 2020; Xiong and Chen 2022). As a result, the infection risk associated with outdoor spaces remains largely unknown, particularly in densely populated urban environments where high-rise buildings can significantly reduce wind dilution capacity (Chen et al. 2021).

While outdoor infectious transmission is considered generally low-risk, some studies suggest possible COVID-19 transmission at outdoor locations (e.g., jogging tracks, parks, and construction sites) (Leclerc et al. 2020; Qian et al. 2021). Although the exact infection location is inconclusive, outdoor places are expected to be open with greater wind speeds than indoors. However, urban canyons with buildings on both sides of a street are both common (Nicholson 1975) and known to have high concentrations of airborne material linked to the sources, airflow and dispersion patterns inside (Wang et al. 2011; Fan et al. 2022; Zheng et al. 2022). As canyons have different street widths and building heights, many combinations occur creating complex, flow and dispersion patterns within

(Li et al. 2006; Tominaga and Stathopoulos 2013). Understanding how such complex urban flows could impact infectious disease transmission is still limited.

Recent studies focus on droplet transmission dynamics inside a 2D street canyon under different wind speed and relative humidity conditions, but quantitative assessment of the associated risk is not provided (Fan et al. 2022). Within street canyon recirculation patterns are influenced by the approach wind speed and people's thermal plumes. These are believed to be crucial factors for droplet dispersion inside the canyon, but the impact of building height to street width ratio (aspect ratio) has not been examined (Yang et al. 2021a). Solar radiation heating of building walls and ground heating can significantly impact ventilation and recirculation within street canyons (Yang et al. 2021b), but has not been addressed in studies (Fan et al. 2022).

Currently, no research explores the relationship between urban morphology and infection risk. This is needed to inform the development of infection-resilient urban design and planning strategies. To fill this gap, our study combines

the Wells-Riley model and computational fluid dynamics (CFD) simulations to evaluate the risk of outdoor airborne infections within 2D urban street canyons. We propose a model to provide an understanding of airborne infection risk patterns across varying aspect ratios, wind velocity and urban heating. To provide context, we compare our findings to typical indoor environments, where there is an established understanding of the relationship between ventilation and airborne transmission risk.

2 Methodology

2.1 Governing equations for CFD simulations

The airflow within the 2D street canyon is characterized as non-isothermal, and the associated buoyancy effects resulting from wall/ground heating are taken into account. The time-averaged quantities are computed using the Reynolds-averaged Navier–Stokes equations (RANS) with the RNG k-ε turbulence model. The commercial CFD software Ansys Fluent v18.1 is employed in this work (Ansys 2017).

The velocity, concentration and thermal fields are described by the mass continuity, momentum, scalar, and energy equations (Ansys 2017):

$$\frac{\partial \overline{u}_i}{\partial x_i} = 0 \tag{1}$$

$$\overline{u}_j \frac{\partial \overline{u}_i}{\partial x_j} = \left(\frac{\rho - \rho_0}{\rho_0}\right)g - \frac{1}{\rho}\frac{\partial \overline{P}}{\partial x_i} - \frac{\partial}{\partial x_j}\overline{u'_i u'_j} \tag{2}$$

$$\overline{u}_j \frac{\partial \overline{c}}{\partial x_j} = \frac{\partial}{\partial x_j}\left(K_c \frac{\partial \overline{c}}{\partial x_j}\right) + S_c \tag{3}$$

$$\overline{u}_j \frac{\partial \overline{\theta}}{\partial x_j} = -\frac{\partial}{\partial x_j}\overline{u'_i \theta'} \tag{4}$$

where the overbars ($\overline{\blacksquare}$) denote the average and primes ($\blacksquare'$) represent the unresolved turbulence quantities. $\overline{u}_i$ and $\overline{u}_j$ are the velocity components and x_i and x_j represent the spatial coordinates. The buoyancy force $\left(\frac{\rho - \rho_0}{\rho_0}\right)g$ in Eq. (2) is modelled using the Boussinesq approximation, and $\rho = \rho_0(1 - \beta(T - T_{ref}))$, in which $\beta = 1/T_{ref}$ is the thermal expansion coefficient, $\beta = 0.00341$ K^{-1} and $T_{ref} = 293.15$ K. For simulation of the pollutant dispersion, carbon monoxide (CO) is used with an emission rate $S_c = 10^{-7}$ kg (m^3 s)$^{-1}$ and a Schmidt number $Sc_t = 0.7$, hence a turbulent diffusivity of pollutant $K_c = \nu/Sc_t$, and θ is the potential temperature. All other terms are defined in the notation list.

The Reynolds stress tensor $\overline{u'_i u'_j}$ is modelled based on the Boussinesq hypothesis as a function of the mean velocity gradients and closure is obtained by the RNG k-ε

turbulence model, which provides equations for the turbulent kinetic energy k and turbulent kinetic energy dissipation rate ε (Ansys 2017):

$$-\overline{u'_i u'_j} = \nu_t\left(\frac{\partial \overline{u}_j}{\partial x_i} + \frac{\partial \overline{u}_i}{\partial x_j}\right) - \frac{2}{3}k\delta_{ij} \tag{5}$$

$$\nu_t = C_\mu k^2 / \varepsilon \tag{6}$$

$$\overline{u}_i \frac{\partial k}{\partial x_i} = \frac{\partial}{\partial x_j}\left(\alpha_k \nu_t \frac{\partial k}{\partial x_j}\right) + P_k + P_b - \varepsilon \tag{7}$$

$$\overline{u}_i \frac{\partial \varepsilon}{\partial x_i} = \frac{\partial}{\partial x_j}\left(\alpha_\varepsilon \nu_t \frac{\partial \varepsilon}{\partial x_j}\right) + C_1 \frac{\varepsilon}{k}\left(P_k + C_3 P_b\right)$$
$$- \left[C_2 + \frac{C_\mu \eta^3 (1 - \eta / \eta_0)}{1 + \gamma \eta^3}\right]\frac{\varepsilon^2}{k} \tag{8}$$

where the model parameters are $C_\mu = 0.0845$, $\alpha_k = \alpha_\varepsilon = 1.393$, $C_1 = 1.42$, $C_2 = 1.68$, $\eta_0 = 4.38$, $\gamma = 0.012$, $C_3 = \tanh(u_2/u_1)$, and u_2 and u_1 are the parallel and perpendicular velocity components related to the gravitational vector, respectively (Ansys 2017). The turbulent kinetic energy production due to mechanical shear is $P_k = -\overline{u'_i u'_j}\frac{\partial u_i}{\partial x_j}$ and the generation of turbulence by buoyancy is $P_b = -\beta g \frac{\nu_t}{Pr_t}\frac{\partial \overline{T}}{\partial x_i}$, where Pr_t is the turbulent Prandtl number for energy.

The second-order upwind scheme is employed to solve all variables and pressure and velocity equations are coupled by using the SIMPLE (Semi-Implicit Method for Pressure-Linked Equations) scheme for coupling pressure and velocity. The under-relaxation factors for the pressure term, momentum term, k, ε and energy terms are 0.3, 0.7, 0.8, 0.8 and 1, respectively. Convergence is considered to be achieved for residuals under 10^{-8} for all variables.

2.2 Computational domain and boundary conditions

This study models a 2D domain with a single street canyon oriented perpendicular to the approaching wind direction, and it is located within an urban boundary layer (Figure 1(a)). We select a 2D street canyon as it represents a worst-case scenario in the context of canyon ventilation (Chen et al. 2021) and can be found widely in most European cities. Full-scale dimensions are used with street width $W = 10$ m that remains constant for all simulations. However, the building height (H) changes, and the aspect ratio is therefore modified to represent different cases. The model domain width is of $3W$ and the height of $5W + H$ (see Figure 1(a)), which satisfies the best practice requirements in urban wind CFD simulation (Tominaga et al. 2008).

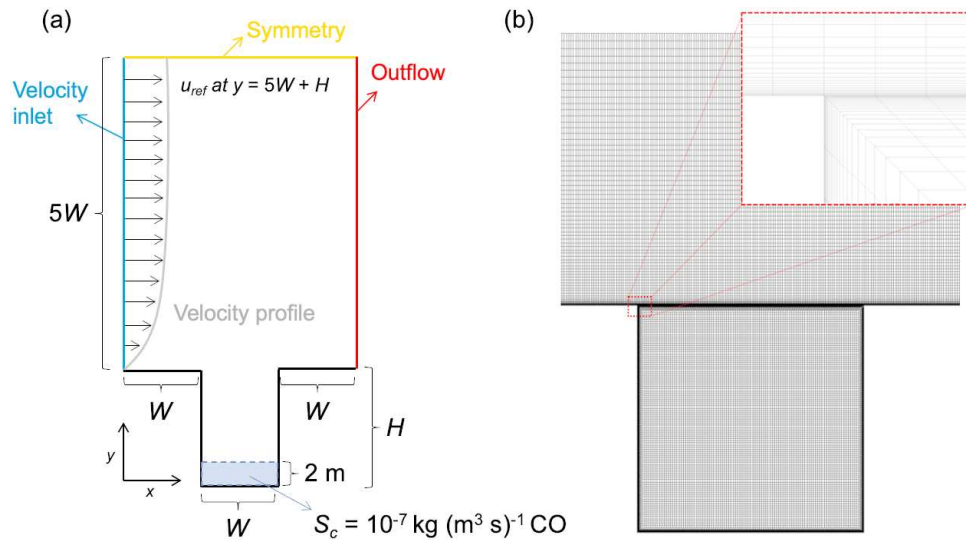The 2D computational domain is discretized into

Fig. 1 Model simulation setup uses a (a) 2D street canyon (e.g., shown AR = 1.5) with domain size specified by height (H) and width (W), where the latter is held constant (W = 10 m). The boundary conditions for the inlet (blue line), top (yellow) and outlet (red), with prescribed uniform tracer emission rate (S_c) at pedestrian level (blue area). Within the canyon, there is a (b) constant grid size (0.1 m), above there is an expansion rate of 1.02, and near-wall refinement with $y^+ < 5$ (dashed red box). The reference height (at u_{ref}) is for both windspeed and the ambient air temperature from which the ΔT values are assigned

rectangular cells inside the canyon and above the building top, as shown in Figure 1(b). A constant square grid size of 0.1 m × 0.1 m is used inside the canyon, while the grid size increases with an expansion rate of 1.02 above the canyon. The enhanced wall function is employed to model the buoyancy effects caused by wall heating, as described in previous studies (Lin et al. 2016; Yang et al. 2021c). The first cell is placed at a distance of 1 mm from the wall to ensure that the viscous sublayer is properly modelled, with a dimensionless wall distance $y^+ < 5$.

At the domain inlet, the velocity profile from a wind tunnel model (Allegrini et al. 2013) is used, with u_{ref} set at the domain top ($y = 5W + H$). Arbitrary initial conditions for turbulent kinetic energy (*TKE*) and *TKE* dissipation rate are set assuming 10% intensity and a turbulent length scale of 1 m. The canyon ground, walls and roofs are defined with no-slip condition (stationary wall) and zero normal gradient is imposed at the top and outlet (outflow) (Figure 1(a)). Heated facets are given a constant temperature, which is higher than the non-heated facets (e.g., roof) set as adiabatic.

2.3 Infection risk model

The Wells-Riley model is used to quantify airborne infection, where quanta account for the number of infectious airborne particles needed to infect a person (Wells 1934). The inhalation of a quantum corresponds to a probability of infection of 63% (1 − 1/e) and the quantum generation rate is a combination of pathogen infectivity and the

infectious source strength in the outbreak. The model (Eq. (9)) considers transmission only through airborne infectious particles and assumes a spatially and temporally uniform distribution of pathogen-laden aerosols in the indoor space:

$$P_{indoor} = 1 - \exp\left(-\frac{Iqpt}{Q}\right) \tag{9}$$

where P_{indoor} is the indoor infection risk, I is the number of infectors [person], p is the pulmonary ventilation rate [m³ s⁻¹], q is the quanta generation rate [quanta (s person)⁻¹], t is the exposure time interval [s], Q is the room ventilation rate with clean air [m³ s⁻¹]. The model, first used to understand a measles outbreak (Riley et al. 1978), is now widely used for airborne infection risk assessment (Andrews et al. 2013; Zhang et al. 2018; Kurnitski et al. 2021; Wang et al. 2022).

Indoor infection risk has been calculated for many typical scenarios e.g., educational settings, retail stores, offices and restaurants (Shen et al. 2021). A minimum air ventilation rate (Q_{min}) can be determined based on floor (ground) area and location (indoor) occupancy, following the ASHRAE 62.1 standard (ASHRAE 2007), which represents the minimum ventilation rate required to maintain good indoor air quality. The ventilation rate factor γ is calculated as Q/Q_{min} to determine the ventilation efficiency from the minimum ventilation required for each space, and it could vary in our calculations (see Figure 9). Table 1 summarises the input parameters used in the indoor scenarios risk assessment.

Table 1 Dimensions for typical indoor spaces (Shen et al. 2021) used with Eq. (9) to assess the indoor infection risk (P_{indoor})

Location	Floor area [m²]	Height [m]	Volume [m³]	Q_{min} [m³ h⁻¹]
Bedroom [a]	36.8	3.0	110.4	14.40
Living room [a]	50.0	3.0	150	24.75
Classroom [b]	99.0	4.0	396	210.96
Library [b]	840.1	4.0	3360.4	642.69
Auditorium [b]	1134	14.6	16556.4	5436.18
Dormitory room [b]	21.5	3.0	64.5	10.35
Large store [c]	348.4	5.2	1811.7	189.81
Small store [c]	174.2	5.2	905.8	94.95
Open office [d]	191.9	2.7	518.1	74.34
Enclosed office [d]	42.3	2.7	114.2	15.93
Ordinary restaurant [e]	371.7	3.0	1115.1	1190.25
Fast-food [e]	116.1	3.0	348.3	371.07

[a] Long-term care facility; [b] Educational setup; [c] Retail store; [d] Office; [e] Restaurant

Here, we modify the Wells-Riley model (Eq. (9)) to assess outdoor infection risk in street canyons, by using a purging flow rate (Q_{PFR}) to represent ventilation in the urban environment:

$$P_{outdoor} = 1 - \exp\left(-\frac{Iqpt}{Q_{PFR}}\right) \tag{10}$$

Although many indices exist to quantify urban ventilation and pollutant dilution capacity (Peng et al. 2020), Q_{PFR} can assess dilution capacity and pollutants removal for a whole area (Hang et al. 2015). The index gives the effective ventilation rate and is independent of the tracer emission rate and can be determined by Eq. (11) (Bady et al. 2008):

$$Q_{PFR} = \frac{S_c \cdot V}{<\overline{c}>} \tag{11}$$

where S_c is tracer emission rate [kg (m³ s)⁻¹], V is the volume [m³] into which the tracer gas is homogeneously emitted, and $<\overline{c}>$ is the spatial and temporal mean concentration [kg m⁻³] in volume V (see list of symbols for notations used in this study). Here, in our CFD set-up, we use a tracer gas (carbon monoxide, CO) emitted uniformly within the pedestrian space ($y = 0 \rightarrow 2$ m, Figure 1), with S_c set to 10^{-7} kg (m³ s)⁻¹ to ensure little disturbance to the flow (Hang et al. 2015).

The use of Q_{PFR} [m³ s⁻¹] as a ventilation index is reasonable since Wells-Riley equations assume well-mixed air and a steady-state infectious particle concentration which is determined by ventilation rate. Larger Q_{PFR} values indicate more effective ventilation and lower infectious aerosol concentration in the pedestrian zone.

2.4 Description of the cases

Outdoor infection risks are calculated for 10 street canyon aspect ratios (AR = 0.33 → 5.0), three approaching wind speeds (at u_{ref} (Figure 1(a)) of 0.5, 2, 4 m s⁻¹) and three heated facets, i.e., street ground, windward wall and leeward wall (when AR = 1, 5 and u_{ref} = 2 m s⁻¹) based on the facet–approaching wind temperature differences (ΔT = 2, 5 and 10 K, Figure 2).

The approaching air (at u_{ref}) temperature is kept constant at 293.15 K and the non-heated facets have a zero-heat flux. Temperature differences of 9–14 K have been observed in street canyons in the summertime in both France (Idczak et al. 2007) and Greece (Santamouris et al. 1999), and have been used as maximum values in previous 2D CFD modelling studies (Hang et al. 2020; Yang et al. 2021c). The parameters used in the different simulation cases (for each AR) are listed in Table 2, including u_{ref} and ΔT alongside the respective total grid cells.

For both the indoor (Eq. (9)) and outdoor risk calculations (Eq. (10)), the epidemiological parameters are kept constant to allow comparison between the cases: I = 1 person (number of infectors), q = 1.4×10^{-3} quanta (s person)⁻¹
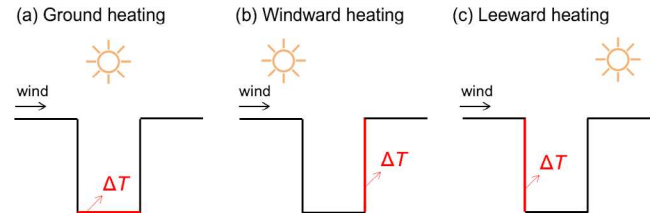

Fig. 2 Three non-isothermal cases prescribed by temperature differences (ΔT) between the facet and ambient air at u_{ref} (held constant at 293.15 K): (a) ground (b) windward wall and (c) leeward wall

Table 2 Simulations, referred to by their aspect ratio (AR), are undertaken for different approaching wind velocities (u_{ref}) and temperature differences (ΔT) between the facet and ambient air. The latter is held constant at 293.15 K at u_{ref} (Figure 1). The total number of grid cells used in each simulation is given

AR	u_{ref} [m s⁻¹]	ΔT [K]	Total grid cells
0.33	0.5, 2, 4	0	51564
0.5	0.5, 2, 4	0	54200
0.75	0.5, 2, 4	0	58150
1	0.5, 2, 4	0, 2, 5, 10	61200
1.5	0.5, 2, 4	0	68500
2	0.5, 2, 4	0	75800
2.5	0.5, 2, 4	0	83400
3	0.5, 2, 4	0	90700
4	0.5, 2, 4	0	105000
5	0.5, 2, 4	0, 2, 5, 10	119300

(quanta emission rate) corresponding to a person speaking (Buonanno et al. 2020), $p = 1.4 \times 10^{-4}$ m^3 s^{-1} (pulmonary ventilation for respiration of susceptible person) (Buonanno et al. 2020) and $t = 3600$ s (exposure time).

3 Results and discussion

3.1 Grid sensitivity and numerical model evaluation

Figure 3 shows the grid sensitivity tests undertaken for three grid sizes namely coarse ($W/50$), medium ($W/100$) and fine ($W/160$). The grid sensitivity is assessed by comparing the vertical profile of normalized velocity along two locations at $x = 0.33W$ and $0.66W$ away from the leeward wall. Qualitative analysis suggests a medium grid size of 0.1 m provides greater computational efficiency (cf. fine grid) without losing accuracy, and higher accuracy results (cf. coarse grid), and is therefore chosen for all the CFD simulations.

Comparison of CFD simulations and wind tunnel measurements of normalized velocity u and TKE profiles along the canyon centreline (Allegrini et al. 2013) have good agreement (Figure 4). Notably, for the u profiles between $y = 0.2H$ to $0.8H$ (Figure 4(a)), but the model underestimates for $y < 0.2H$ and slightly overestimates for $y > 0.8H$. The simulated TKE profile for $y < 0.4H$ more evidently underestimates (Figure 4(b)), but beyond that, there is good agreement with experimental data. The result is consistent with prior street canyon ventilation CFD studies
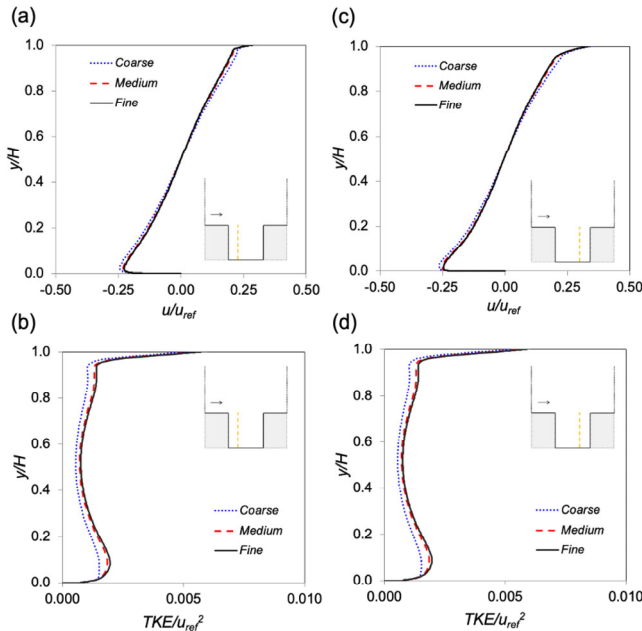

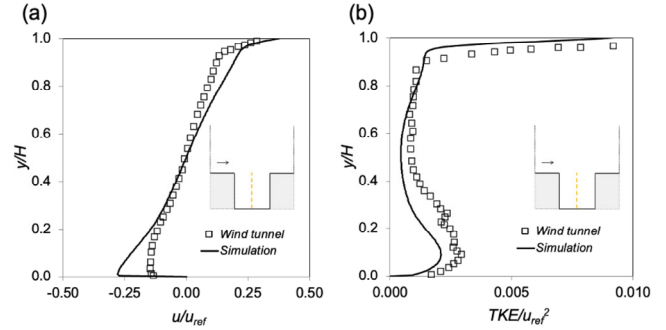**Fig. 4** Vertical profiles of (a) normalized velocity (u) and (b) turbulent kinetic energy (TKE) for the current simulation using medium grid and wind tunnel observations (Allegrini et al. 2013) in the centre of the canyon (inset) for a street canyon with AR = 1

(Ding et al. 2019; Fan et al. 2022). The discrepancy is probably due to RANS's turbulent viscosity tendency to overpredict the mean and underpredict the fluctuations and its poorer ability to predict separated shear flows (cf. high-order models) (Blocken 2018).

In addition to the qualitative analysis based on Figure 4, the accuracy of the simulation results is quantitatively estimated using common metrics used in similar CFD studies (Schatzmann et al. 2010; Hood et al. 2021; Zhang et al. 2022).

(1) Factor-of-2 of observations (FAC2):

$$\text{FAC2} = \frac{1}{N}\sum_{i=1}^{N} n_i,$$

$$\text{where } n_i = \begin{cases} 1 & \text{for } 0.5 \leq \dfrac{P_i}{O_i} \leq 2 \\ 1 & \text{for } O_i \leq W_a \text{ and } P_i \leq W_a \\ 0 & \text{else} \end{cases} \tag{12}$$

(2) Pearson correlation coefficient (R):

$$R = \frac{\sum_{i=1}^{N}\left(P_i - \overline{P}\right)\left(O_i - \overline{O}\right)}{\sqrt{\sum_{i=1}^{N}\left(P_i - \overline{P}\right)^2}\sqrt{\sum_{i=1}^{N}\left(O_i - \overline{O}\right)^2}} \tag{13}$$

(3) Normalised mean absolute error (nMAE):

$$\text{nMAE} = \frac{\overline{\left|P_i - O_i\right|}}{\overline{O}} \tag{14}$$

(4) Normalised mean squared error (nMSE):

$$\text{nMSE} = \frac{\overline{\left(P_i - O_i\right)^2}}{\overline{P\,O}} \tag{15}$$

(5) Normalised mean bias error (nMBE):

Fig. 3 Vertical profiles of (a, c) normalized velocity (u) and (b, d) turbulent kinetic energy (TKE) for two locations (inset) of the street canyon with AR = 1 using coarse ($W/50 = 0.2$ m), medium ($W/100 = 0.1$ m) and fine ($W/160 = 6.25 \times 10^{-3}$ m) grids

$$\text{nMBE} = \frac{\overline{(P_i - O_i)}}{\overline{O}} \qquad (16)$$

where N is the number of data points and W_a (= 0.05) is the allowed absolute deviation, $\overline{P}$ the mean of the simulation's values, $\overline{O}$ is the mean of the wind tunnel observations (Allegrini et al. 2013) and i the individual values.

Table 3 presents the calculated values of evaluation metrics for velocity (u) and turbulent kinetic energy (TKE) alongside the acceptable criteria. This study adopts the following criteria: FAC2 > 0.5, nMSE < 1.5, and R > 0.8 as recommended by previous studies (Chang and Hanna 2004; Moonen and Allegrini 2015). The normalized mean squared error (nMSE) is 0.148 for velocity with little underestimation (nMBE < 0.200) in the vertical region of $0.2 < y/H < 0.4$. the nMSE = 1.409 for turbulent kinetic energy, which is slightly below the acceptable criteria (nMSE < 1.5), but still consistent with other similar CFD studies (Di Sabatino et al. 2011). These combined metrics provide further confidence

Table 3 Assessment metrics for velocity (u) and turbulent kinetic energy (TKE) with their ideal values and acceptable criterion

	FAC2	R	nMAE	nMSE	nMBE
Ideal value	1	1	0	0	0
Acceptable criterion	> 0.5	> 0.8	—	< 1.5	—
u (m s^{-1})	0.618	0.977	0.285	0.148	−0.385
TKE (m^2 s^{-2})	0.543	0.870	0.574	1.409	−0.570

in our 2D simulation results compared with experimental measurements.

3.2 Impact of street canyon aspect ratio and approaching wind speed

The impact of aspect ratio (AR) on the purging flow rate (Q_{PFR}) and the resultant infection risk is investigated while keeping a constant wind speed at the top of the canyon (e.g., u_{ref} = 0.5 m s^{-1}, Figure 5(a)). Deeper canyons, which have larger AR or taller buildings (Figures 5(e)–(f)), experience slower wind speeds near the ground due to the above canyon flow taking longer to reach the ground. This reduces both dilution rates and the removal capacity of infectious aerosols. Overall, the Q_{PFR} decreases with the increase of AR, but the outdoor infection risk increases sharply for street canyons with AR ≥ 3, indicating significantly lower near-ground ventilation capacity in deeper canyons compared to shallower canyons (Figures 5(a)–(c)). The risk can be relatively low (< 5%) for street canyons with AR < 4, suggesting a similar single vortex pattern (Figures 5(d)–(e), cf. Figure 5(f)) inside the canyon promoting similar dilution capacity. However, the risk can be as high as 30% inside deeper canyons with AR = 5 under low wind speeds (u_{ref} = 0.5 m s^{-1}), suggesting that deeper canyons are more vulnerable to outdoor infection risk.

The approaching wind speed (u_{ref}) has a significant impact on both the purging flow rate (Q_{PFR}) and the outdoor
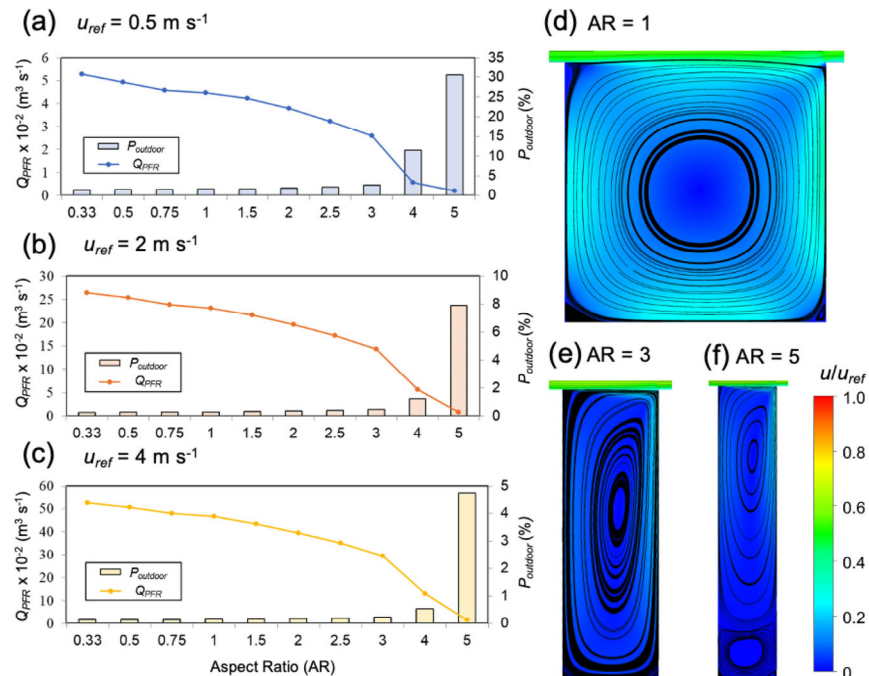

Fig. 5 Q_{PFR} (lines) and $P_{outdoor}$ (bars) for street canyons for 10 aspect ratios (AR) for approaching wind speed at domain top (u_{ref}, Figure 1(a)) set to (a) 0.5 m s^{-1}, (b) 2 m s^{-1} and (c) 4 m s^{-1} (note y-scales differ between plots); and airflow streamlines inside the canyon when u_{ref} = 2 m s^{-1} and AR equal to (d) 1, (e) 3 and (f) 5

infection risk ($P_{outdoor}$). The risk decreases consistently with increasing u_{ref} (Figures 5(a)–(c)), indicating an approximately 10-fold decrease in the Q_{PFR} inside the canyon for most cases from u_{ref} = 4 m s^{-1} to 0.5 m s^{-1} (e.g., Q_{PFR} decreases from 0.465 m s^{-1} to 0.045 m s^{-1} for AR = 1). This decrease in the Q_{PFR} may be accentuated for deeper canyons (AR > 3) due to the formation of multiple vortex patterns inside the canyon (Figure 5(f)) and can reach 20-fold for AR = 4. Table 4 shows Q_{PFR} and $P_{outdoor}$ simulated for different aspect ratios (AR) and approaching wind speeds (u_{ref}) for the isothermal case.

3.3 Impact of individual facet heating

In non-isothermal conditions, the local buoyancy as well as the approaching wind speed magnitude have an impact on the airflow inside a street canyon. For a street canyon with AR = 1 and u_{ref} = 2 m s^{-1}, we consider three different heated facets: ground, leeward and windward wall. Figure 6 shows that there is a gradual increase in Q_{PFR} as the buoyancy increases for the heated ground and leeward cases, indicating an improvement in the canyon ventilation (cf. isothermal case) leading to reduced infection risk. The infection risk reduction can be up to 27.4% and 24.1%, for a temperature difference of 10 K between approaching airflow and ground and leeward walls, respectively. These heating patterns accelerate vortex rotation via buoyancy-assisted wind-driven flow (Cai 2012; Mei and Yuan 2022). Whereas the vortex rotation is suppressed due to the thermally driven flow opposing the downwash flow from the canyon top generated from the windward wall heating (Buccolieri et al. 2022), potentially leading to poorer in-canyon ventilation and higher infection risk (i.e., 0.5% for windward heating and 10 K temperature difference).

Table 4 Q_{PFR} and $P_{outdoor}$ for street canyons with different aspect ratios (AR) and approaching wind speeds (u_{ref}) for the isothermal case

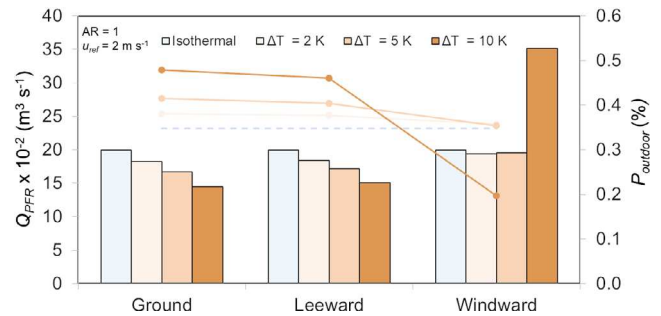|	u_{ref} = 0.5 m s^{-1}		u_{ref} = 2 m s^{-1}		u_{ref} = 4 m s^{-1}	
AR	Q_{PFR} [m^3 s^{-1}]	$P_{outdoor}$ [%]	Q_{PFR} [m^3 s^{-1}]	$P_{outdoor}$ [%]	Q_{PFR} [m^3 s^{-1}]	$P_{outdoor}$ [%]
0.33	0.053	1.31	0.265	0.26	0.526	0.13
0.5	0.049	1.40	0.254	0.27	0.506	0.14
0.75	0.046	1.50	0.239	0.29	0.479	0.14
1	0.045	1.54	0.232	0.30	0.465	0.15
1.5	0.042	1.63	0.216	0.32	0.434	0.16
2	0.038	1.82	0.196	0.35	0.395	0.18
2.5	0.032	2.13	0.172	0.40	0.350	0.20
3	0.026	2.65	0.144	0.48	0.295	0.24
4	0.006	11.46	0.057	1.22	0.131	0.53
5	0.002	30.60	0.008	7.89	0.014	4.75

Fig. 6 Q_{PFR} (lines) and $P_{outdoor}$ (bars) for a street canyon with AR = 1 and approaching wind speed of 2 m s^{-1} with four temperature differences (ΔT = 0, 2, 5, and 10 K, colour) for ground, leeward and windward heated facets

For a canyon with AR = 1 and a u_{ref} = 2 m s^{-1}, increasing the temperature of the ground and leeward facets (from 2 to 10 K) results in a slightly stronger inner recirculation (Figure 7). Similarly, when the windward wall is heated by 5 K (cf. approaching airflow temperature) the buoyancy force is insufficient to disrupt the predominant skimming flow, leading to a slightly lower Q_{PFR} (cf. 0 K case). However, the upward buoyancy force predominates (cf. downward airflow) when the windward wall temperature difference is ΔT = 10 K (Lin et al. 2016), disrupting the usual canyon vortex (Figure 7(i)) and decreasing Q_{PFR} considerably. Although there is little change in outdoor risk for heated windward case ΔT from 0 to 5 K, the infection risk increases by 75% inside the canyon when ΔT =10 K (Figure 6).

There is a more noticeable reduction in the infection risk for all heated facets for a canyon with AR = 5 and a u_{ref} =
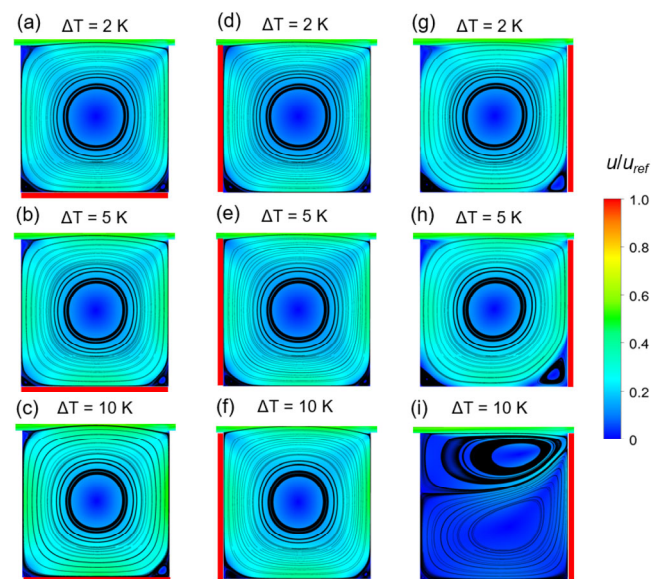

Fig. 7 Flow field and streamlines for a street canyon with AR = 1 and approaching wind speed of 2 m s^{-1} with different heated facets (a–c) ground, (d–f) leeward and (g–i) windward, with temperature differences higher than the approaching airflow temperature of (a, d, g) 2 K, (b, e, h) 5 K and (c, f, i) 10 K

2 m s^{-1} (Figure 8(a), cf. canyon with AR = 1, Figure 6). The reduction in risk is due to the increased relative buoyancy force, which offsets the weakened airflow near the ground. Increasing the facet's temperature from 0 to 2 K compared to the airflow temperature leads to a stronger inner recirculation and lower infection risk. When the ground is heated with a temperature difference of $\Delta T = 10$ K, a multi-vortex flow structure is formed inside the canyon (Figure 8(b)), which traps aerosol particles near the ground and decreases the removal capacity. As a result, the infection risk is greater when the ground is heated (cf. heated leeward and windward facets). Although street canyons with AR = 5 have a higher infection risk than with AR = 1, the latter is very common in cities (Nicholson 1975) and windward wall heating can increase infection risk for pedestrians walking in these areas, which is relevant to public health considerations.

3.4   Comparison to indoor risk

For the infection risk in indoor spaces, we evaluated five different indoor spaces with varying levels of ventilation rate factor ($\gamma = Q/Q_{min}$) ranging from poorly ventilated ($\gamma = 0.5$) to well-ventilated ($\gamma = 2$). Our results indicate that dormitory rooms have the highest risks, while auditoriums

have the lowest risks with $P_{indoor} = 21.46\%$ and 0.05%, respectively, when $\gamma = 1$ (Figure 9). This difference can be mainly attributed to the variations in floor area and volume of the indoor spaces (see Table 1). Although auditoriums may have more occupants than other indoor spaces, they also present higher maximum ventilation rates, which leads to lower risks in these locations.

When considering outdoor cases, Figure 9 shows that the infection risk can be as high as 30.6% for a street canyon with AR = 5 when the approaching wind speed (u_{ref}) is 0.5 m s^{-1}. This risk level is comparable to dormitory rooms with very poor ventilation. For AR = 4, the risk is 11.46%, which is similar to the risk levels found in typical indoor locations such as open offices or fast-food restaurants (Figure 9). Therefore, our results demonstrate that deep canyons may pose a significant risk to individuals engaging in outdoor activities, especially on calm wind days, and can be comparable to typical indoor spaces in terms of infection risk. However, the outdoor risk decreases considerably for lower aspect ratios, reaching 2.65% for a street canyon with AR = 3 with approaching wind speed equal to 0.5 m s^{-1} (see Table 4). These results have important implications for public health and urban planning and suggest the need for effective measures to mitigate the risk of airborne transmission in outdoor settings.
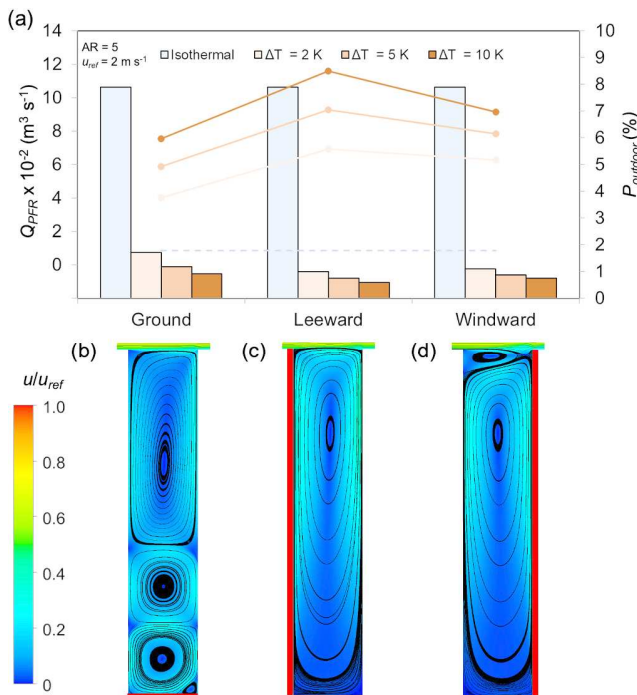

Fig. 8 Q_{PFR} (lines) and $P_{outdoor}$ (bars) for street canyon with AR = 5 and approaching wind speed of 2 m s^{-1} (a) with four temperature differences ($\Delta T = 0$, 2, 5, and 10 K, colours). The plots below are the flow field and streamlines for (b) ground, (c) leeward and (d) windward, with temperature differences higher than the approaching airflow temperature of 10 K
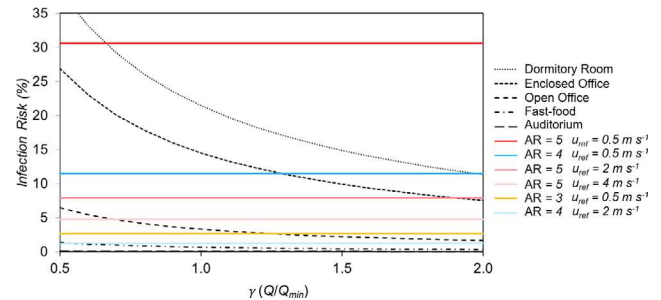

Fig. 9 Infection risk for indoor (dashed black, see Table 1 for parameters) and outdoor street canyons with different AR under isothermal flow (colour)

4   Limitations of this study

We follow best practices for CFD simulations and for methodological assumptions but limitations still could affect the results:

- Two-dimensional (2D) modelling can accurately represent street canyon airflow and aerosol dispersion features if the approaching wind speed is perpendicular to the street axis (Zheng et al. 2021). This situation typically has the poorest dispersion because the ventilation capacity increases with oblique wind directions (Zhang et al. 2016; Jon et al. 2023). It is important to consider worst-case scenarios in risk assessments. However, 2D simulations

will not capture the 3D wind field, such as lateral wind circulation around a 3D urban structure (Mei et al. 2019). Hence, it is recommended future studies include 3D simulations with different wind directions.

- This study has focused on ventilation as a means of controlling and removing infectious particles from outdoor environments. However, it is worth noting that other processes can also contribute to the removal of these particles, including droplet deposition on surfaces such as the ground and building walls, ultraviolet (UV) radiation and precipitation (Jones et al. 2021; He et al. 2022). Further studies should assess the individual importance of these processes.

- Whilst we analyse the impact of the bulk ventilation capacity on the infection risk, other in-canopy elements, such as traffic, can affect the flow and dispersion patterns of infectious particles, and hence, the interpersonal transmission. This effect can be especially pronounced at low wind speeds when car movement can create a piston effect (Zheng and Yang 2022).

- The Wells-Riley model is widely used for estimating the risk of airborne infectious disease transmission. However, this model assumes well-mixed conditions, which may not accurately reflect the complex and dynamic airflow patterns that occur in outdoor environments. While acknowledging this limitation, the Wells-Riley model can still provide valuable insights and contribute to the understanding of infectious disease transmission in urban environments.

5   Conclusions

In this study, the outdoor risk of airborne infection is investigated by using the Wells-Riley model and CFD simulations of 2D urban street canyons under various conditions of aspect ratios, wind velocities and urban heating patterns. The results we report contradict the general view that outdoor spaces are safer zones compared to indoors with plentiful ventilation and dilution capacity. Although shallow street canyons may not represent a high outdoor infection risk, deep and poorly ventilated street canyons could pose a high COVID-19 infection risk. Street canyons with AR > 3 have a similar COVID-19 infection risk as that in poorly ventilated indoor spaces. The infection risk can be reduced through local heating of ground and leeward walls, which improves in-canyon ventilation. However, the infection risk may increase by 75% when the windward wall is heated up to 10 K compared to ambient air. In these cases, passive ventilation enhancers, such as void decks (Chew and Norford 2018), could be an effective method to mitigate flow stagnation near the ground within deep canyons and potentially reduce the risk.

This study focuses on the often-overlooked outdoor infection risk. We highlight the critical need for a comprehensive understanding of factors influencing the transmission of airborne infectious diseases in urban environments. Our findings demonstrate outdoor infection risk should not be overlooked, and that urban morphology is a significant factor in the control and mitigation of outdoor airborne infectious disease transmission. Prediction of outdoor environments infection risk can inform decision-making and promote public health and safety. Public health officials, event planners, employers, city planners, and individuals can use our proposed model to assess disease transmission risk and take appropriate measures to protect the community. Further research and development of this tool are warranted to enhance our understanding of outdoor environment infectious disease transmission and to improve our ability to prevent and control disease outbreaks.

Acknowledgements

References

Allegrini J, Dorer V, Carmeliet J (2013). Wind tunnel measurements of buoyant flows in street canyons. *Building and Environment*, 59: 315–326.

Andrews JR, Morrow C, Wood R (2013). Modeling the role of public transportation in sustaining tuberculosis transmission in South Africa. *American Journal of Epidemiology*, 177: 556–561.

Ansys (2017). Ansys Fluent Theory Guide 18.1. Ansys Inc.

ASHRAE (2007). ASHRAE Standard 62.1-2007. Ventilation for Acceptable Indoor Air Quality. Atlanta, GA, USA: American Society of Heating, Refrigerating and Air-Conditioning Engineers.

Bady M, Kato S, Huang H (2008). Towards the application of indoor ventilation efficiency indices to evaluate the air quality of urban areas. *Building and Environment*, 43: 1991–2004.

Blocken B (2018). LES over RANS in building simulation for outdoor and indoor applications: A foregone conclusion? *Building Simulation*, 11: 821–870.

Bourouiba L (2020). Turbulent gas clouds and respiratory pathogen emissions: Potential implications for reducing transmission of COVID-19. *JAMA*, 323: 1837–1838.

Buccolieri R, Carlo OS, Rivas E, et al. (2022). Obstacles influence on existing urban canyon ventilation and air pollutant concentration: a review of potential measures. *Building and Environment*, 214: 108905.

Bulfone TC, Malekinejad M, Rutherford GW, et al. (2021). Outdoor transmission of SARS-CoV-2 and other respiratory viruses: a systematic review. *The Journal of Infectious Diseases*, 223: 550–561.

Buonanno G, Stabile L, Morawska L (2020). Estimation of airborne viral emission: Quanta emission rate of SARS-CoV-2 for infection risk assessment. *Environment International*, 141: 105794.

Cai X (2012). Effects of differential wall heating in street canyons on dispersion and ventilation characteristics of a passive scalar. *Atmospheric Environment*, 51: 268–277.

Chang JC, Hanna SR (2004). Air quality model performance evaluation. *Meteorology and Atmospheric Physics*, 87: 167–196.

Chen L, Hang J, Chen G, et al. (2021). Numerical investigations of wind and thermal environment in 2D scaled street canyons with various aspect ratios and solar wall heating. *Building and Environment*, 190: 107525.

Cheng P, Luo K, Xiao S, et al. (2022). Predominant airborne transmission and insignificant fomite transmission of SARS-CoV-2 in a two-bus COVID-19 outbreak originating from the same pre-symptomatic index case. *Journal of Hazardous Materials*, 425: 128051.

Chew LW, Norford LK (2018). Pedestrian-level wind speed enhancement in urban street canyons with void decks. *Building and Environment*, 146: 64–76.

Di Sabatino S, Buccolieri R, Olesen HR, et al. (2011). COST 732 in practice: The MUST model evaluation exercise. *International Journal of Environment and Pollution*, 44: 403–418.

Ding S, Huang Y, Cui P, et al. (2019). Impact of viaduct on flow reversion and pollutant dispersion in 2D urban street canyon with different roof shapes - Numerical simulation and wind tunnel experiment. *Science of the Total Environment*, 671: 976–991.

Fan X, Zhang X, Weerasuriya AU, et al. (2022). Numerical investigation of the effects of environmental conditions, droplet size, and social distancing on droplet transmission in a street canyon. *Building and Environment*, 221: 109261.

Hang J, Wang Q, Chen X, et al. (2015). City breathability in medium density urban-like geometries evaluated through the pollutant transport rate and the net escape velocity. *Building and Environment*, 94: 166–182.

Hang J, Chen X, Chen G, et al. (2020). The influence of aspect ratios and wall heating conditions on flow and passive pollutant exposure in 2D typical street canyons. *Building and Environment*, 168: 106536.

He M, Fang K, Zhou F, et al. (2022). A delayed modulation of solar ultraviolet radiation on the COVID-19 transmission reflects an incubation period. *Meteorological Applications*, 29(5): e2099.

Hood C, Stocker J, Seaton M, et al. (2021). Comprehensive evaluation of an advanced street canyon air pollution model. *Journal of the Air and Waste Management Association*, 71: 247–267.

Idczak M, Mestayer P, Rosant JM, et al. (2007). Micrometeorological measurements in a street canyon during the joint ATREUS-PICADA experiment. *Boundary-Layer Meteorology*, 124: 25–41.

James A, Eagle L, Phillips C, et al. (2020). High COVID-19 attack rate among attendees at events at a church—Arkansas, March 2020. *MMWR Morbidity and Mortality Weekly Report*, 69: 632–635.

Jon KS, Luo Y, Sin CH, et al. (2023). Impacts of wind direction on the ventilation and pollutant dispersion of 3D street canyon with balconies. *Building and Environment*, 230: 110034.

Jones B, Sharpe P, Iddon C, et al. (2021). Modelling uncertainty in the relative risk of exposure to the SARS-CoV-2 virus by airborne aerosol transmission in well mixed indoor air. *Building and Environment*, 191: 107617.

Kurnitski J, Kiil M, Wargocki P, et al. (2021). Respiratory infection risk-based ventilation design method. *Building and Environment*, 206: 108387.

Leclerc QJ, Fuller NM, Knight LE, et al. (2020). What settings have been linked to SARS-CoV-2 transmission clusters? *Wellcome Open Research*, 5: 83.

Li X, Liu CH, Leung DYC, et al. (2006). Recent progress in CFD modelling of wind field and pollutant transport in street canyons. *Atmospheric Environment*, 40: 5640–5658.

Li Y, Qian H, Hang J, et al. (2021). Probable airborne transmission of SARS-CoV-2 in a poorly ventilated restaurant. *Building and Environment*, 196: 107788.

Lin L, Hang J, Wang X, et al. (2016). Integrated effects of street layouts and wall heating on vehicular pollutant dispersion and their reentry toward downstream canyons. *Aerosol and Air Quality Research*, 16: 3142–3163.

Mei S, Luo Z, Zhao F, et al. (2019). Street canyon ventilation and airborne pollutant dispersion: 2-D versus 3-D CFD simulations. *Sustainable Cities and Society*, 50: 101700.

Mei S, Yuan C (2022). Urban buoyancy-driven air flow and modelling method: A critical review. *Building and Environment*, 210: 108708.

Moonen P, Allegrini J (2015). Employing statistical model emulation as a surrogate for CFD. *Environmental Modelling and Software*, 72: 77–91.

Nicholson SE (1975). A pollution model for street-level air. *Atmospheric Environment* (*1967*), 9: 19–31.

Peng Y, Buccolieri R, Gao Z, et al. (2020). Indices employed for the assessment of "urban outdoor ventilation"—A review. *Atmospheric Environment*, 223: 117211.

Qian H, Miao T, Liu L, et al. (2021). Indoor transmission of SARS-CoV-2. *Indoor Air*, 31: 639–645.

Qin H, Lin P, Lau SSY, et al. (2020). Influence of site and tower types on urban natural ventilation performance in high-rise high-density urban environment. *Building and Environment*, 179: 106960.

Riley EC, Murphy G, Riley RL (1978). Airborne spread of measles in a suburban elementary school. *American Journal of Epidemiology*, 107: 421–432.

Santamouris M, Papanikolaou N, Koronakis I, et al. (1999). Thermal and air flow characteristics in a deep pedestrian canyon under hot weather conditions. *Atmospheric Environment*, 33: 4503–4521.

Schatzmann M, Olesen HR, Franke J (2010). COST 732 model evaluation case studies: Approach and results.

Shen J, Kong M, Dong B, et al. (2021). A systematic approach to estimating the effectiveness of multi-scale IAQ strategies for reducing the risk of airborne infection of SARS-CoV-2. *Building and Environment*, 200: 107926.

Tominaga Y, Mochida A, Yoshie R, et al. (2008). AIJ guidelines for practical applications of CFD to pedestrian wind environment around buildings. *Journal of Wind Engineering and Industrial Aerodynamics*, 96: 1749–1761.

Tominaga Y, Stathopoulos T (2013). CFD simulation of near-field pollutant dispersion in the urban environment: A review of current modeling techniques. *Atmospheric Environment*, 79: 716–730.

Wang P, Zhao D, Wang W, et al. (2011). Thermal effect on pollutant dispersion in an urban street Canyon. *International Journal of Environmental Research*, 5: 813–820.

Wang Z, Galea ER, Grandison A, et al. (2022). A coupled Computational Fluid Dynamics and Wells-Riley model to predict COVID-19 infection probability for passengers on long-distance trains. *Safety Science*, 147: 105572.

Wells WF (1934). On air-borne infection: Study II. Droplets and droplet nuclei. *American Journal of Epidemiology*, 20: 611–618.

WHO (2023). WHO Coronavirus. Available at https://www.who.int/health-topics/coronavirus

Xiong Y, Chen H (2022). Impacts of uneven surface heating of an ideal street canyon on airflows and indoor ventilation: numerical study using OpenFOAM coupled with EnergyPlus. *Building Simulation*, 15: 265–280.

Yang X, Yang H, Ou C, et al. (2021a). Airborne transmission of pathogen-laden expiratory droplets in open outdoor space. *Science of the Total Environment*, 773: 145537.

Yang H, Chen G, Wang D, et al. (2021b). Influences of street aspect ratios and realistic solar heating on convective heat transfer and ventilation in full-scale 2D street canyons. *Building and Environment*, 204: 108125.

Yang H, Lam CKC, Lin Y, et al. (2021c). Numerical investigations of re-independence and influence of wall heating on flow characteristics and ventilation in full-scale 2D street canyons. *Building and Environment*, 189: 107510.

Zhang H, Xu T, Wang Y, et al. (2016). Study on the influence of meteorological conditions and the street side buildings on the pollutant dispersion in the street canyon. *Building Simulation*, 9: 717–727.

Zhang N, Huang H, Su B, et al. (2018). A human behavior integrated hierarchical model of airborne disease transmission in a large city. *Building and Environment*, 127: 211–220.

Zhang X, Weerasuriya AU, Wang J, et al. (2022). Cross-ventilation of a generic building with various configurations of external and internal openings. *Building and Environment*, 207: 108447.

Zheng X, Montazeri H, Blocken B (2021). Large-eddy simulation of pollutant dispersion in generic urban street canyons: Guidelines for domain size. *Journal of Wind Engineering and Industrial Aerodynamics*, 211: 104527.

Zheng X, Montazeri H, Blocken B (2022). Impact of building façade geometrical details on pollutant dispersion in street canyons. *Building and Environment*, 212: 108746.

Zheng X, Yang J (2022). Impact of moving traffic on pollutant transport in street canyons under perpendicular winds: A CFD analysis using large-eddy simulations. *Sustainable Cities and Society*, 82: 103911.